The Astrophysical Journal, 708:1–8, 2010 January 1 doi:10.1088/0004-637X/708/1/1

CHANDRA OBSERVATIONS OF THE RADIO GALAXY 3C 445 AND THE HOT SPOT X-RAY EMISSION MECHANISM

Eric S. Perlman[1], Markos Georganopoulos[2,3], Emily M. May[4,5], and Demosthenes Kazanas[3]
[1] Department of Physics and Space Sciences, Florida Institute of Technology, 150 W. University Blvd., Melbourne, FL 32901, USA
[2] Department of Physics, University of Maryland-Baltimore County, 1000 Hilltop Circle, Baltimore, MD 21250, USA
[3] Laboratory for High Energy Astrophysics, NASA Goddard Space Flight Center, Code 661, Greenbelt, MD 20771, USA
[4] Department of Physics and Astronomy, University of Wyoming, WY 82071, USA
[5] Southeastern Association for Research in Astronomy (SARA) NSF-REU Summer Intern at Florida Institute of Technology, USA
Received 2009 August 14; accepted 2009 October 19; published 2009 December 8

ABSTRACT

We present new *Chandra* observations of the radio galaxy 3C 445, centered on its southern radio hot spot. Our observations detect X-ray emission displaced upstream and to the west of the radio–optical hot spot. Attempting to reproduce both the observed spectral energy distribution and the displacement excludes all one-zone models. Modeling of the radio–optical hot spot spectrum suggests that the electron distribution has a low-energy cutoff or break approximately at the proton rest mass energy. The X-rays could be due to external Compton scattering of the cosmic microwave background coming from the fast (Lorentz factor $\Gamma \approx 4$) part of a decelerating flow, but this requires a small angle between the jet velocity and the observer's line of sight ($\theta \approx 14^{\circ}$). Alternatively, the X-ray emission can be synchrotron from a separate population of electrons. This last interpretation does not require the X-ray emission to be beamed.

Key words: galaxies: active – galaxies: individual (3C 445) – galaxies: jets – radio continuum: galaxies – X-rays: galaxies

1. INTRODUCTION

The hot spots of powerful Fanarof–Rilley type II (FR II; Fanaroff & Riley 1974) radio galaxies and quasars are the locations where the jets of these sources, after propagating for distances up to ∼1 Mpc, terminate in a collision with the intergalactic medium. The optical emission observed in several hot spots suggests that at least a fraction of the electrons that goes through the shock(s) formed at the termination of the jets undergoes efficient particle acceleration (Heavens & Meisenheimer 1987; Meisenheimer et al. 1989; Prieto et al. 2002). *Chandra* results show that while in some sources (e.g., Cygnus A; Wilson et al. 2000) the hot spot X-ray emission is consistent with synchrotron-self-Compton radiation from relativistic electrons in energy equipartition with the magnetic field (SSCE), in other sources (e.g., the hot spot on the jet side of Pictor A; Wilson et al. 2001; Hardcastle & Croston 2005; Migliori et al. 2007; Tingay et al. 2008) the X-ray emission is at a much higher level (by up to a factor of ∼1000). The nature of this anomalously bright (significantly brighter than SSCE) X-ray hot spot emission remains a matter of active discussion in the literature, being connected to the issue of particle acceleration efficiency and jet power (for two recent reviews see Harris & Krawczynski 2006 and Worrall 2009) and extending to a similar and possibly related issue for the knots of powerful jets (e.g., Kataoka & Stawarz 2005).

Two different considerations appear to be relevant to the collective properties of hot spot X-ray emission, relativistic beaming, and hot spot luminosity; however, it is not as yet clear how exactly these may be combined to reproduce the observed phenomenology. Based on early *Chandra* results, suggesting that in most cases the anomalously bright X-ray hot spots were seen at the approaching jet of sources with jets forming relatively small angles to the observer's line of sight, Georganopoulos & Kazanas (2003) proposed that the X-ray emission is beamed, and that the plasma in the hot spot is relativistic and decelerating from a bulk Lorentz factor $\Gamma \sim 2$–3 to velocities that match the subrelativistic advance speed of lobes ($u/c \approx 0.1$; Arshakian & Longair 2000). In this scenario, the X-ray emission is mostly due to upstream Compton (UC) scattering of electrons in the upstream fast ($\Gamma \sim 2$–3) part of the flow, inverse Compton (IC) scattering the synchrotron photons produced downstream. The relevance of beaming is also supported by a study of quasar hot spots by Tavecchio et al. (2005) that concluded that the anomalously bright X-ray emission is indeed found mostly on the hot spot corresponding to the approaching-jet side, although these authors favor the cosmic microwave background (CMB) as a source of seed photons. On the other hand, Hardcastle et al. (2004) find only weak evidence that the anomalously X-ray bright hot spots are more frequently found at the termination of the approaching jet.

The second consideration, namely, the hot spot luminosity, was introduced by Brunetti et al. (2003), who found that the synchrotron emission seen at radio energies extends to the optical for lower power sources like 3C 445 (Prieto et al. 2002) but cuts off before the optical regime for powerful sources like Cygnus A (Wilson et al. 2000). They explained this as a consequence of radiative losses increasing with hot spot luminosity. The luminosity range over which this decrease of the synchrotron peak frequency with increasing luminosity is observed, was extended to powerful hot spots by Cheung et al. (2005). Based on an extensive sample of hot spot multiwavelength data, Hardcastle et al. (2004) argued for the relevance of the hot spot luminosity to the X-ray emission, by showing that hot spots with X-ray luminosity much higher than that predicted by SSCE were usually of low luminosity, in contrast to more powerful hot spots. However, instead of UC, Hardcastle et al. (2004) favored synchrotron emission from an altogether separate electron population as the source of the anomalously bright X-ray emission. Other workers have also come to the conclusion that synchrotron radiation from a second electron population is the most likely emission mechanism for

this component (e.g., in the case of Pic A; see Fan et al. 2008; Tingay et al. 2008), partly as a result of observing compact radio hot spots with the Very Long Baseline Array (VLBA).

Synchrotron radiation, but from a single electron population, is indeed the X-ray emission mechanism for the jets of low power FR I radio galaxies, as seen from their single component radio–optical–X-ray spectra (e.g., Perlman & Wilson 2005 for the jet of M87). This turns out to be the case also for some of the weakest host spots of FR II radio galaxies: for example, the northern hot spot of 3C 390.3 (Hardcastle et al. 2007), the northern hot spots of 3C 33 (Kraft et al. 2007), the eastern hot spots of 3C 403 (Kraft et al. 2007), and both hot spots of 0836+299 (Tavecchio et al. 2005). It comes as no surprise that in these sources their X-ray emission is much higher than the anticipated SSC flux, since the X-ray emission is indeed the continuation of the radio–optical synchrotron spectrum to higher energies. We therefore do not consider sources that exhibit a single spectral component from radio to X-ray emission to be part of the family of hot spots exhibiting anomalously high X-ray emission.

An additional handle in understanding the X-ray emission process of the anomalously X-ray bright hot spots (those for which the X-rays (1) cannot be a continuation of the synchrotron spectrum and (2) are significantly brighter than predicted by SSCE) can come from spatial displacements between the emission at different frequencies. In a handful of these hot spots, displacements between the radio and the X-ray hot spot emission have been observed, with the X-rays being upstream of the radio: 3C 351 (Hardcastle et al. 2002), 4C 74.26 (Erlund et al. 2007), 3C 390.3 and 3C 227 (Hardcastle et al. 2007), 3C 321 (Evans et al. 2008), and 3C 353 (Kataoka et al. 2008). So far no displacements have been observed in the hot spots of sources for which their X-ray emission is consistent with SSCE. An additional important characteristic is that when optical–IR emission is detected from these hot spots (as in 3C 227, 3C 390.3, and 3C 351), it coincides with or is shifted somewhat upstream of the radio, to a location downstream of the X-rays. Beaming in the hot spots that exhibit displacements can be a relevant but not a dominant influence, because, while in three of them the hot spots are in the approaching jet that points toward us (4C 74.26, 3C 227, and 3C 351), in two others (3C 321 and 3C 353), the jets are believed to be close to the plane of the sky, while in superluminal 3C 390.3 the hot spot exhibiting the X-ray radio displacement is at the termination of the counter jet. Similarly, a low hot spot power does not seem to be strictly required, since the hot spot of 3C 351 is rather powerful and still exhibits the displacements mentioned above.

In this paper, we present *Chandra* X-ray observations and discuss the X-ray emission mechanism of the hot spots of 3C 445, a broad line FR II radio galaxy at redshift $z = 0.0562$ (Eracleous & Halpern 1994), which for the standard cosmology ($H_0 = 71$ km s^{-1} Mpc^{-1}, $\Omega_\Lambda = 0.73$, and $\Omega_M = 0.27$) corresponds to a luminosity distance of 247.7 Mpc. This is a promising source for constraining the hot spot X-ray emission mechanism with high-resolution *Chandra* observations. Both its southern and northern hot spots have been detected in the radio and in the near-IR/optical, with the southern hot spot being ∼3 times brighter than the northern and having multiple sites of synchrotron optical emission, a manifestation of ongoing particle acceleration (Prieto et al. 2002; Mack et al. 2009). The hot spot–counter hot spot luminosity difference can be intrinsic, or due to mild beaming with the southern hot spot being on the approaching-jet side.

In the first case, adopting the suggestion of Hardcastle et al. (2004), we expect X-ray emission brighter than SSCE from both hot spots, because this is a source with a modest extended power at 178 MHz, $P_{178} = 3.0 \times 10^{25}$ W Hz^{-1} sr^{-1} (Hardcastle et al. 1998), as well as a low 5 GHz luminosity from both hot spots ($L_{5\,\mathrm{GHz}} = 3.4 \times 10^{22}$ W Hz^{-1} sr^{-1} for the northern hot spot and $L_{5\,\mathrm{GHz}} = 7.9 \times 10^{22}$ W Hz^{-1} sr^{-1} for the southern hot spot; Mack et al. 2009). In this scenario, the X-ray emission from the weaker northern hot spot is expected to be higher than predicted by the X-ray to radio ratio from the brighter southern hot spot. This model makes no prediction regarding offsets between emission in different bands.

In the second case, we expect that due to beaming, the presumed approaching-jet side, southern hot spot will have more pronounced X-ray emission. In the context of a relativistic decelerating hot spot flow (Georganopoulos & Kazanas 2003, 2004), we also expect to observe offsets, with the X-rays peaking upstream of the radio. If, in addition, distributed particle acceleration takes place (as suggested by Prieto et al. 2002), the optical and radio emission will peak at the same location (see Figure 3 of Georganopoulos & Kazanas 2004).

3C 445 has been the subject of several X-ray observations. *GINGA* observations were reported by Pounds (1990), while *ASCA* observations were reported by Sambruna et al. (1998). Both observations reported an absorbed Seyfert nucleus with a hard X-ray continuum. *XMM-Newton* observations of 3C 445 were previously published by Sambruna et al. (2007) and Grandi et al. (2007), but in those data a partial window configuration was chosen for the MOS and pn that caused both the northern and southern hot spots to be at locations where the CCDs were not read out. This work thus represents the first study of extended X-ray emission from this object, and we report the discovery of X-ray emission from the southern hot spot, as well as a meaningful X-ray flux upper limit from the northern hot spot. In Section 2, we discuss the *Chandra* observations, as well as the data reduction and analysis procedures. In Section 3, we present and contrast the morphology seen in each band for the southern hot spot. In Section 4, we discuss the X-ray emission mechanism of the southern hot spot, present our conclusions, and suggest directions for future work.

2. OBSERVATIONS AND DATA REDUCTION

3C 445 was observed with the Advanced CCD Imaging Spectrometer (ACIS) on the *Chandra X-ray Observatory* on 2007 October 18 for 50 ks. The ACIS-S configuration was used due to its linear alignment which allowed all emission regions (in particular both hot spots) to be included in the observation. The northern and southern hot spots are at projected distances of ∼300 kpc (more than 5 arcmin in angular distance) from the core of the galaxy. However, because of the greater surface brightness of the southern hot spot (seen in the radio and near-IR), we decided to center it in the observations to maximize our sensitivity and angular resolution in this region.

The *Chandra* observations were reduced in the Chandra Interactive Analysis of Observations (CIAO) software package. Standard recipes (i.e., the science threads) were followed for imaging spectroscopy of extended sources as well as data preparation and filtering. No significant flare events were seen during the observation, so all data could be used in the analysis. We extracted spectra for the southern hot spot and nucleus, and created an exposure map to allow a search for emission from other source regions. All X-ray spectra were fitted in XSPEC. This process is discussed in Section 3.

Deep optical and near-infrared observations of the northern and southern hot spots were obtained by Prieto et al. (2002) with the Very Large Telescope (VLT) of the European Southern Observatory (ESO) and the Infrared Spectrometer and Array Camera (ISAAC) in the K_S (2.2 μm), H (1.7 μm), J_S (1.2 μm), and I (0.9 μm) bands; deeper images in these same bands plus the R (0.7 μm) and B (0.45 μm) bands were obtained by Mack et al. (2009). We refer the reader to those papers for a discussion of their data reduction procedures. We obtained near-IR and optical fluxes from their paper, as well as from Mack et al. (2009). We obtained their VLT J_S-band image for use in this paper.

We extracted radio data for 3C 445 from the NRAO data archives. 3C 445 was observed with the NRAO Very Large Array (VLA) on 2002 September 9, at both 8.5 and 5.0 GHz. The VLA was in the B configuration, yielding a clean beam (resolution element) of 0.82 × 0.72 arcsec in P.A. 77°.44. Those data were originally analyzed by Brunetti et al. (2003); we reanalyze them in this paper. Data reduction was done in AIPS, using standard procedures. We also obtained radio fluxes in other bands from Brunetti et al. (2003).

In registering the three data sets to a common frame of reference, we assumed the VLA map to be the fiducial, adhering to the usual IAU standard. The VLT image was registered to this frame by comparing to Palomar Sky Survey and USNO-A2.0 data. The radio galaxy itself could not be used for this procedure, as it was out of the field of view of both the VLT and VLA images. It was therefore necessary to use stars in the field to do the registration. We then checked the alignment of the radio and optical images by overplotting the two, in the process reproducing the Prieto et al. (2002) overlay. Following this, the 1σ errors in the positions from the VLT image are $\pm 0\farcs2$ in R.A. and decl. (see, e.g., Deutsch 1999) relative to either the radio or X-ray images, while those in the X-ray image are $\pm 0\farcs4$,[6] relative to either the radio or optical.

3. RESULTS

Both the northern and southern hot spots of 3C 445 are seen in multiple optical/near-IR bands (Prieto et al. 2002; Mack et al. 2009). However, X-ray emission was seen from the southern hot spot only. In Table 1, we list all fluxes for both hot spots, using all available data. In Figure 1, we show the X-ray, radio, and near-IR images of the southern radio hot spot. The radio and near-IR images are shown both at the pixel scale of the *Chandra* data (i.e., $0\farcs492$ pixel^{-1}; middle and bottom left panels) as well as at the finer pixel scale of the VLA image (i.e., $0\farcs220$ pixel^{-1}, middle and bottom right panels). Our *Chandra* observations detect about 200 counts from the southern hot spot. The X-ray emission extends along a $6''$ region, extending very nearly east–west and peaking near the middle or perhaps slightly to the west of its center point.

There are clear differences between the morphologies seen in the near-IR, X-ray, and radio (Figure 1). In contrast to the X-ray emission, in the near-IR and radio we see a concave arc, which appears to contain the X-ray emission in its hollow part. This can be seen in Figure 1's left-hand panels, which show the data at a common pixel scale. There also appear to be offsets between the position of the X-ray emission component and those seen in the near-IR and radio. Looking at higher resolution (middle right and bottom right panels), the near-IR emission breaks up into three discrete regions, which we term NIR 1–3 in east–west order, shown also in Mack et al. (2009). The brightest near-IR emission is located within region NIR 1. The radio emission peak is also near this position, and the higher-resolution VLA data of Mack et al. (2009) show that the radio emission shows a broad plateau that includes the entire maximum region of NIR 1.

We have attempted to quantify the displacements between components in different bands by fitting elliptical Gaussians to each major component within AIPS, using the task JMFIT. In order to utilize the full resolution of our data, we did this measurement at the native resolution in each band, using small boxes to zero in on the visible maxima. These positions are reported in Table 2, and are also compared in the top right-hand panel of Figure 1. In the case of the near-IR emission, we report three centroids, one for each of the three regions NIR 1–3. We report in Table 2 with parentheses the internal errors from JMFIT (estimated at 0.2 pixels where smaller values were reported). However, for cross-comparison between bands, we must emphasize that the errors are dominated by the uncertainty in registration between bands, i.e., $\sim 0\farcs2$–$0\farcs4$, as detailed in Section 2. Note that these are errors in cross-comparison, i.e., they do not constitute errors on each individual position but rather get added only once to the internal errors reported in Table 2. As can be seen, the displacement between the X-ray and radio peak is significant at $>3\sigma$, while the displacements between the X-ray peak and those of NIR 1 and NIR 2 are at the 2.4σ–3σ level.

Our *Chandra* data include the position of the northern hot spot, which was detected for the first time in the near-IR by Mack et al. (2009), who describe its radio and optical morphology. We do not detect it in the *Chandra* image, and the flux quoted in Table 1 reflects a 3σ upper limit. Note that due to the northern hot spot's off-center location, the sensitivity of *Chandra* was reduced by about 60% at this position.

Table 1
Hot Spot Fluxes

Feature	Telescope	Flux (μJy)	Frequency (Hz)	Source
3C 445 N	VLA	4000000	74×10^8	4
3C 445 N	VLA	1400000	330×10^8	4
3C 445 N	VLA	160000	1.4×10^9	2
3C 445 N	VLA	58000	4.8×10^9	2
3C 445 N	VLA	35000	8.4×10^9	2
3C 445 N	VLT	7.2 ± 2.2	1.38×10^{14}	2
3C 445 N	VLT	<2.9	1.81×10^{14}	2
3C 445 N	VLT	2.4 ± 0.7	2.47×10^{14}	2
3C 445 N	*Chandra*	$<2.60 \times 10^{-4}$	1.21×10^{18}	3
3C 445 S	VLA	7900000	74×10^8	4
3C 445 S	VLA	2000000	330×10^8	4
3C 445 S	VLA	520000	1.4×10^9	1
3C 445 S	VLA	135000	4.8×10^9	1
3C 445 S	VLA	81000	8.4×10^9	1
3C 445 S	VLT	16.5 ± 1.5	1.38×10^{14}	2
3C 445 S	VLT	15.2 ± 3.0	1.81×10^{14}	2
3C 445 S	VLT	13.6 ± 1.4	2.47×10^{14}	2
3C 445 S	VLT	5.65 ± 0.57	3.33×10^{14}	2
3C 445 S	VLT	4.56 ± 0.90	4.29×10^{14}	2
3C 445 S	VLT	2.95 ± 0.60	6.82×10^{14}	2
3C 445 S	VLT	0.95 ± 0.19	8.33×10^{14}	2
3C 445 S	*Chandra*	9.38×10^{-4}	1.21×10^{18}	3

References. (1) Brunetti et al. 2003; (2) Mack et al. 2009; (3) this paper; (4) Kassim et al. 2007 and N. E. Kassim 2009, private communication.

[6] See the *Chandra* Science Thread on Astrometry, http://cxc.harvard.edu/cal/ASPECT/celmon.

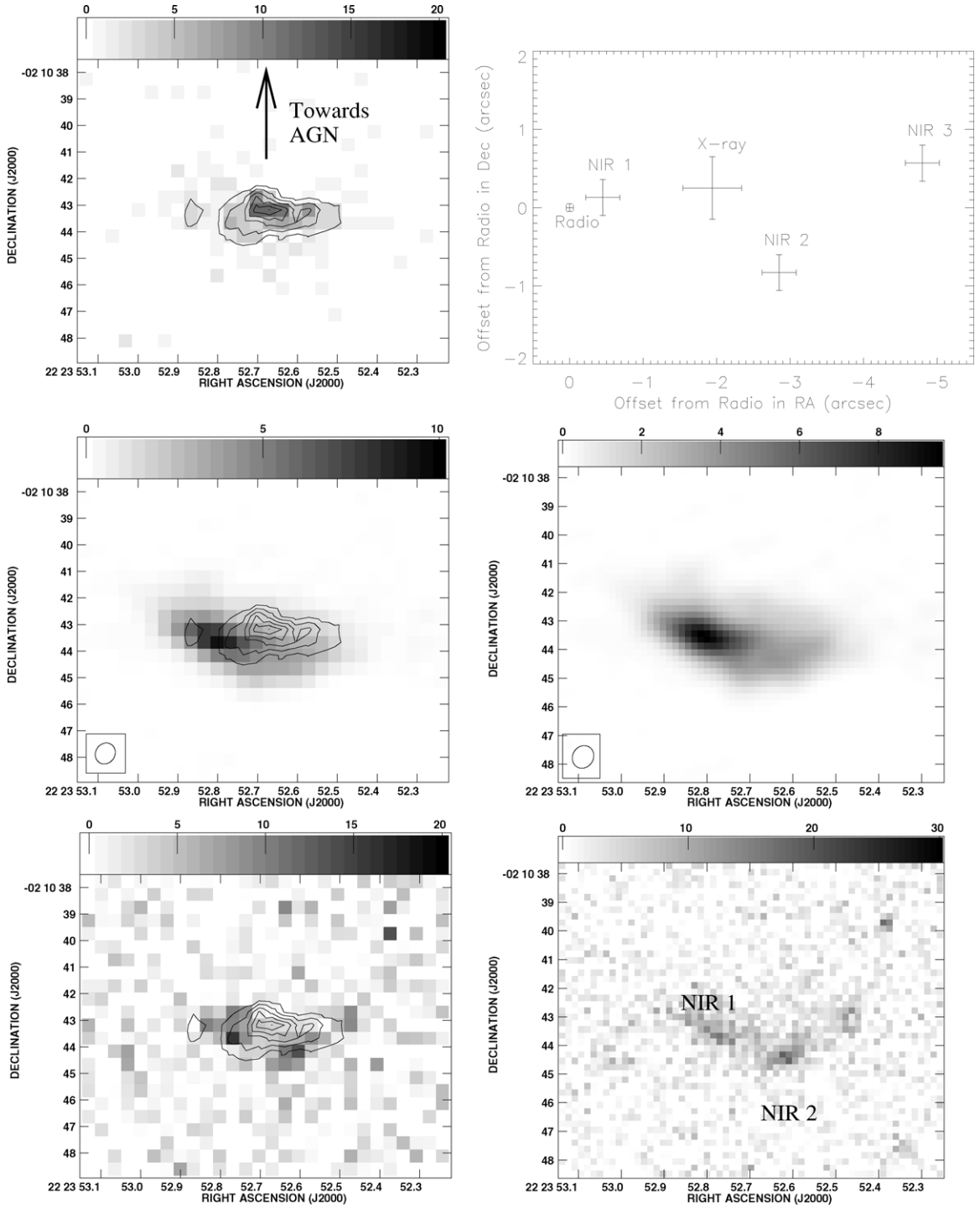

Figure 1. Southern hot spot of 3C 445, as seen in the X-rays (top left panel), radio (middle panels), and near-IR (bottom panels). The images at left were resampled to 0.″492 pixel^{-1}, while the middle right and bottom right panels are at 0.″220 pixel^{-1}. The contours were taken from the *Chandra* image, smoothed with a 1-pixel (FWHM) Gaussian. Contours are plotted at 2, 4, 6,. . ., counts pixel^{-1}. The top right panel shows the centroid of the emission components in each band, plotted with error bars relative to the radio frame. See Section 3 for discussion.

We extracted an X-ray spectrum for the southern hot spot of 3C 445, using *specextract* in CIAO. In order to create the spectra of the AGN, we defined two regions in ds9: the hot spot and a background region that was free from other sources. This allowed us to create a series of files, including source and background PI spectra, weighted ARF and RMF files, FEF weight files, and a grouped spectrum. The energy range was left unrestricted for both source spectra. Following this step, XSPEC was used to fit both the spectra of the hot spot and the active galactic nucleus (AGN). Here, we discuss the spectral fits and broadband spectrum of the southern hot spot only, as the AGN was off-center for these observations and our results for it are fully consistent with those of Sambruna et al. (2007) and Grandi et al. (2007).

The southern hot spot's X-ray spectrum was easily modeled by a basic power law with fixed galactic absorption $N_H^{\rm Gal} = 5.33 \times 10^{20}$ cm^{-2}, a photon index $\Gamma = 1.95^{+0.38}_{-0.34}$, and a χ^2 value of 0.85, and is shown in Figure 2.

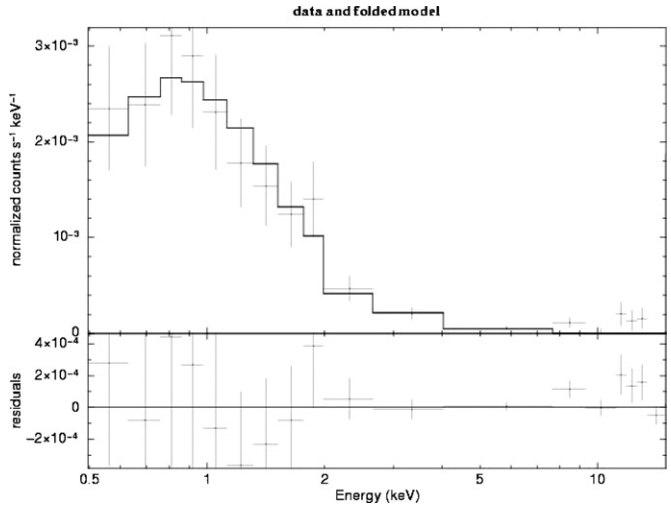

Figure 2. X-ray spectrum of the southern hot spot with the best-fit power law overlaied. Below it are the residuals.

Table 2
Positions of Emission Regions in Southern Hot Spot

Band	R.A. (J2000)	Decl.	Delta (Radio)
X-ray	22 23 52.67 (0.01)	−02 10 43.29 (0.05)	(−1.94,+0.25)
NIR 1	22 23 52.77 (0.01)	−02 10 43.67 (0.12)	(−0.45,+0.13)
NIR 2	22 23 52.61 (0.01)	−02 10 44.37 (0.12)	(−2.85,−0.83)
NIR 3	22 23 52.48 (0.01)	−02 10 42.97 (0.22)	(−4.80,+0.57)
Radio	22 23 52.80 (0.01)	−02 10 43.54 (0.02)	(0,0)

4. DISCUSSION

One of the key results of our *Chandra* observations is that the X-ray emission of the southern hot spot has a very different morphology than that seen in the radio and optical and also shows a likely displacement. This displacement rules out all forms of one-zone models. Before discussing the possible interpretations for the X-ray emission, we turn to the radio and optical emission that are approximately cospatial. The radio–optical spectral energy distribution (SED) of the southern and northern hot spots are plotted in Figure 3, along with the X-ray points. The southern hot spot is brighter in the radio and optical by a factor of ≈3. If we attribute the brightness difference to beaming, we are forced to conclude that the beaming of the radio–optical emitting plasma is mild. Below, we discuss the multiwavelength emissions of both hot spots and model possible X-ray emission mechanisms.

4.1. A High Value of $\gamma_{\rm min}$ in the Radio–Optical Hot Spot?

The southern hot spot's radio–optical SED can be modeled as synchrotron emission from a population of relativistic electrons in energy equipartition with the hot spot magnetic field. Assuming that beaming is not important for the radio–optical emission, the equipartition magnetic field is

$$B_{\rm eq} = \left[\frac{96\pi^2 m_e c L_r \nu_r^{(s-1)/2}\left(\gamma_{\rm min}^{2-s} - \gamma_{\rm max}^{2-s}\right)}{c_1^{(s-3)/2}\sigma_\tau V(s-2)}\right]^{2/(s+5)}, \quad (1)$$

where L_r is the radio luminosity at frequency ν_r, m_e is the electron mass, c is the speed of light, σ_τ is the Thomson cross section, and V is the volume of the emitting region. The injected electron distribution is a power law of index $s = 2\alpha_r + 1 = 2.6$ from Lorentz factor $\gamma_{\rm min}$ to $\gamma_{\rm max}$, with $\alpha_{\rm ro} = 0.9 = \alpha_r$ being

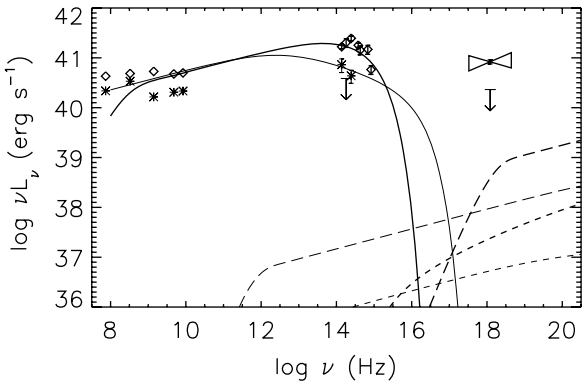

Figure 3. SED of the southern hot spot of 3C 445 is shown with diamonds for the radio and optical and bow-tie for the X-rays. The SED of the northern hot spot is also plotted with asterisks, including the upper limit for the X-ray flux. The data used are taken from Table 1. Due to angular resolution constraints, the three lowest radio frequencies may include lobe emission and should be considered upper limits for the hot spot fluxes. The thin (thick) lines represent emission in equipartition conditions, assuming $\gamma_{\rm min} = 1$ ($\gamma_{\rm min} = 1840$). Solid lines represent the synchrotron, short dash lines the SSC, and long dash lines the EC/CBM emission.

the radio–optical spectral index (Mack et al. 2009). To derive Equation (1), we assumed that an electron of Lorentz factor γ in a magnetic field B radiates most of its energy at the characteristic frequency $\nu = c_1 B\gamma^2$, with $c_1 = e/(2\pi m_e c)$. In Equation (1), $\gamma_{\rm max}$ can in many cases be determined observationally from the maximum observed synchrotron frequency. However, $\gamma_{\rm min}$ is customarily set to a value chosen by hand. As we discuss now, there is a way to determine observationally, or at least constrain the value of $\gamma_{\rm min}$, and through this get a more appropriate value for $B_{\rm eq}$. This in turn affects significantly the level of both the SSC and the external Compton scattering (EC)/CMB emission.

Because in this case $s > 2$ and the synchrotron emission extends for at least six decades in frequency, $\gamma_{\rm max}/\gamma_{\rm min} \gg 1$, to a very good approximation $B_{\rm eq} \propto \gamma_{\rm min}^{-2(s-2)/(s+5)} = \gamma_{\rm min}^{-1.2/7.6}$: an increase in $\gamma_{\rm min}$ results in a mild decrease of $B_{\rm eq}$. There are two observational constraints on $\gamma_{\rm min}$. An upper limit on $\gamma_{\rm min}$ is derived from the fact that it has to be low enough to produce the lowest observed radio frequency from the hot spot $\nu_{r,\rm min} > c_1 B_{\rm eq}\gamma_{\rm min}^2$. A lower limit comes from the fact that there is no sign of radiative cooling in the radio–optical SED, because the optical flux level is found practically on the extrapolation of the radio spectrum. This sets an upper limit on the magnetic field in the radio–optical hot spot (regardless of equipartition arguments), which in turn sets a lower limit on $\gamma_{\rm min}$.

To demonstrate these considerations, in Figure 3 we plot with a thin solid line the synchrotron emission in the case of $\gamma_{\rm min} = 1$. This corresponds to an equipartition magnetic field, $B_{\rm eq} = 70.4$ μG. As can be seen, while the synchrotron SED clearly extends below the lowest radio frequency safely associated with the hot spot (this is the 4.8 GHz point, because the 1.4 GHz point may be contaminated with non-hot-spot emission (see Mack et al. 2009; Prieto et al. 2002), as is also true for the lower frequency points; Kassim et al. 2007), the synchrotron spectrum breaks at $\sim 10^{12}$–10^{13} Hz and by doing so, underproduces the optical emission of the hot spot. This is because the high value of $B_{\rm eq}$ causes a break in the electron energy distribution due to radiative cooling (a cooling break is expected at $\gamma_b = 3m_e c^2/[4\sigma_\tau(B^2/8\pi + U_{\rm CMB})R]$, where $U_{\rm CMB}$ is the energy density of the CMB and R is the size of the hot spot that determines the electron escape time R/c). To fit the

observed SED, we need significantly higher values of $\gamma_{\rm min}$. A value of $\gamma_{\rm min} \approx 1840$ similar to the proton to electron mass ratio m_p/m_e is required to ensure that there is no cooling break signature at frequencies lower than optical. The value of the corresponding equipartition magnetic field is $B_{\rm eq} = 21.5\ \mu$G. We plot the resulting synchrotron SED in Figure 3 with a thick solid line. Note that at low frequencies the model with $\gamma_{\rm min} \approx 1840$ (thick solid line) exhibits a break due to the high value of $\gamma_{\rm min}$ (the slope below the break is due to the $\nu^{1/3}$ synchrotron emissivity of electrons with Lorentz factor $\gamma_{\rm min}$). Note also that this model manages to reproduce the optical emission of the hot spot.

There is practically little freedom for $\gamma_{\rm min}$ around m_p/m_e if we want to model the radio to optical SED with synchrotron in equipartition. Let us mention that observationally driven arguments for similarly high values of $\gamma_{\rm min}$ in hot spots of other radio galaxies have been presented by other astronomers (e.g., Blundell et al. 2006; Stawarz et al. 2007; Godfrey et al. 2009). However, some jet sources require much lower values, e.g., PKS 0637–752 (Mehta et al. 2009). Values of $\gamma_{\rm min} \approx m_p/m_e$ are particularly interesting, because this is the minimum energy that electrons crossing a shock must have to be picked up efficiently by Fermi acceleration (e.g., Spitkovsky 2008). The level of both the EC and SSC emission depends on the value of $B_{\rm eq}$, which in turns depends on $\gamma_{\rm min}$: because $L_{\rm SSC,EC}/L_S \propto U_B^{-1} \propto B^{-2}$, and $B_{\rm eq} \propto \gamma_{\rm min}^{-2(s-2)/(s+5)}$, for $B = B_{\rm eq}$, $L_{\rm SSC,EC} \propto \gamma_{\rm min}^{4(s-2)/(s+5)} = \gamma_{\rm min}^{2.4/7.6}$. Therefore, an increase from $\gamma_{\rm min} = 1$ to $\gamma_{\rm min} = 1840$ should increase the EC and SSC level by a factor of ≈ 10.7, as seen in Figure 3. Even for $\gamma_{\rm min} = 1840$, the X-ray emission of the radio–optical hot spot is much weaker than the upstream detected X-ray emission.

If analyses like the above point toward a high value of $\gamma_{\rm min}$, then future low-frequency–high angular resolution observations (e.g., with the Long Wavelength Array) should detect the SED break at low frequencies. Existing low-frequency radio observations suggest such a break for the eastern hot spot of Cygnus A (Lazio et al. 2006). For 3C 445, VLA observations at 74 MHz and 330 MHz (Kassim et al. 2007) provide us with upper limits for the emission of the hot spots (due to lobe contamination). The low-frequency data plotted in Figure 3 may be contaminated by lobe emissions and hence are not sufficient to constrain the spectral shape below 4.8 GHz. If a low-frequency break is found by future low-frequency-high-resolution observations, they will strengthen the above picture. If on the other hand, the low-frequency radio spectrum exhibits no such break, we will have to search for an alternative reason for the lack of cooling break (as we discussed above, a low value for $\gamma_{\rm min}$, manifested through a lack of low-frequency break, requires a higher value for $B_{\rm eq}$, which in turns produces a cooling break below the optical, as can be seen from the thin solid line in Figure 3). Distributed reacceleration is a very plausible candidate and it has been claimed to explain the optical emission of 3C 445 (e.g., Prieto et al. 2002).

4.2. What is the X-ray Emission Mechanism?

Any interpretation of the X-rays must take into account (1) the level and spectrum of the X-ray emission, (2) the apparent upstream "nesting" of the X-ray emission into the hollow part of the east–west arc of radio–optical emission, and (3) the mostly westward displacement of the X-ray emission relative to the peak of the radio–NIR 1 hot spot. Also, because of the moderate hot spot to counter hot spot flux ratio in the radio and optical,

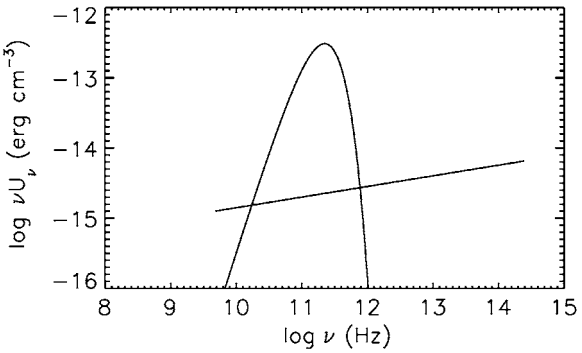

Figure 4. Energy density at the location of the southern hot spot. The straight line represents the photon energy density due to the radio–optical emission of the hot spot, while the blackbody is the CMB.

it should not invoke significant beaming for the radio–optical emitting plasma. These considerations automatically exclude the possibilities of one-zone EC/CMB (Tavecchio et al. 2005) and SSC in equipartition, because in these models both the SSC and EC/CMB emission is cospatial with the radio–optical hot spot emission and (see Figure 3) is much lower than the X-ray detected flux).

A displacement between the X-ray and radio emission is predicted in the case of UC emission from a decelerating flow, in which freshly accelerated relativistic electrons from the fast base of the flow upscatter to high energies the radio photons produced in the downstream slow part of the flow by electrons that have cooled radiatively (Georganopoulos & Kazanas 2003). This version of the UC emission from a decelerating flow is not favored, however, as it predicts that the optical and the X-rays are cospatial and that the radio emission is shifted downstream. This is because optical emission can only be produced by the fast, upstream part of the flow, where the freshly accelerated electrons are found, the same place from where the UC X-rays are produced. Also, the model predicts the optical to be more beamed than the radio, something not supported by the very similar hot spot to counter hot spot flux ratio in radio and optical. Finally, the model uses as seed photons the synchrotron photons produced in the source, making the implicit assumption that these photons dominate the local photon energy density. This is not the case, as can be seen in Figure 4.

The fact that the X-ray emission is displaced from the radio–optical hot spot requires the X-ray emitting electrons to also be displaced from the radio–optical emitting electrons. If the X-ray emission is of IC nature, these electrons will experience the seed photon field of Figure 4, provided they are located at a distance from the radio–optical host spot not much greater than the radio–optical hot spot size. This immediately excludes the IR–optical photons as seed photons for the X-ray emission, because this would require the presence of a powerful component of IC emission due to CMB photons upscattered in $\sim$ the optical band, co-located with the X-ray component. This is not observed. We therefore reach the conclusion that if the X-ray emission is due to a particle population located upstream of those in other bands, then the seed photons that these electrons upscatter must be the CMB.

A model that produces cospatial radio–optical synchrotron emission and EC/CMB X-ray emission shifted upstream has been proposed by Georganopoulos & Kazanas (2004) to address such displacements observed in the large-scale jets of quasars. The model assumes that distributed particle acceleration offsets radiative losses. In this model, a relativistic decelerating flow

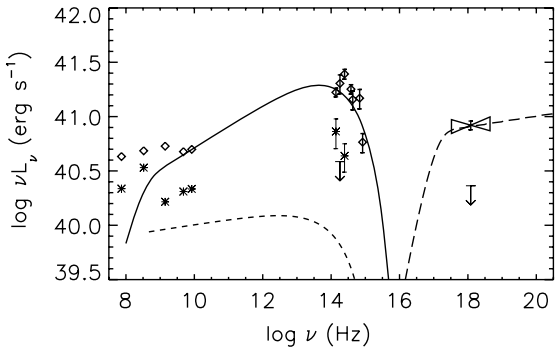

Figure 5. X-rays due to EC/CMB (long dash line). The emission is assumed to come from plasma moving relativistically (bulk Lorentz factor $\Gamma = 4$) at an angle $\theta = 14^\circ$ to the line of sight. To reproduce the observed displacements, we assume that the flow decelerates and bends to $\sim\theta = 30^\circ$ and terminates $\sim$4.6 kpc downstream, producing the radio–optical emission (solid line). The radio–optical emission coming from the X-ray spot is much weaker (short dash line). The data points are the same plotted in Figure 3.

results in an increase of the magnetic field and electron density at the slow downstream part of the flow, increasing the synchrotron emissivity. At the same time, the faster upstream part of the flow experiences a higher CMB comoving energy density $U_{\rm CMB} \propto \Gamma^2$, where Γ is the bulk Lorentz factor of the flow (see Figure 3 of Georganopoulos & Kazanas 2004). In this scenario, the only displacement observed is along the flow axis. In our case, however, besides the general upstream shift of the X-rays relative to the radio–NIR emission, we note that the peak of the radio–NIR 1 emission is shifted by $\sim 2''$ to the east relative to the center of the X-rays ($1''$ corresponds to 1.07 kpc). Therefore, for this model to still be viable, the flow needs to bend to the east after producing the X-ray emission.

To demonstrate how this could reproduce the observed upstream X-ray emission, we plot in Figure 5 the emission that would result from plasma in equipartition moving with a bulk Lorentz factor $\Gamma = 4$ at an angle to the line of sight $\theta = 14^\circ$ and carrying the same power as that injected in the radio–optical hot spot ($L_{\rm kin} = 1.3 \times 10^{44}$ erg s^{-1}). Although such a small angle to the line of sight, bordering angles typical of blazars is admittedly uncomfortable, it cannot be excluded for this broad line FR II radio galaxy. To reproduce the shift of the radio–optical emission in NIR relative to the X-ray emission, the flow must bend to the east, forming an angle of 30° to the line of sight. The projected physical distance between the X-ray and radio–optical components is 4.6 kpc. Bends in the flow and velocity gradients at the hot spots, such as the one suggested here, are seen in numerical simulations of relativistic flows (e.g., Aloy et al. 1999). Deceleration from $\Gamma = 4$ to the subrelativistic speed of the radio–optical hot spot could be achieved by a series of oblique shocks that could also aid electron reacceleration. This latter possibility could be tested by future, high-resolution radio imaging of the hot spot. If indeed this is the X-ray emission mechanism, we expect that due to relativistic dimming, the X-ray emission from the counter hot spot would be undetectable, even for very deep *Chandra* exposures. On the assumption of hot spot–counter hot spot symmetry, X-ray detection of the counter hot spot would exclude this last alternative for an IC interpretation of the X-rays.

An alternative model, which avoids the uncomfortably small jet angle to the line of sight and the relatively high Lorentz factor of the X-ray emitting plasma needed for the above interpretation, together with the arguments against strong beaming in other sources (see Section 1), is to generate the X-ray emission via synchrotron radiation from a high-energy population ($\gamma \sim 10^8$) of electrons accelerated upstream of the radio–optical hot spot. A possible way to produce this electron population upstream the radio–optical emitting region is through acceleration in the reverse shock of a reverse–forward shock structure (in this picture the radio–optical comes from electron acceleration in the forward shock; Kataoka et al. (2008) proposed it, motivated by the upstream, relative to the radio, X-ray emission seen in both hot spots and jets of 3C 353). This scheme, however, as Kataoka et al. (2008) note, does not address the reason the two shocks accelerate electrons at different energies, with the reverse shock consistently reaching higher electron energies. If the X-ray emission of the southern hot spot is synchrotron, then the observed emission in the *Chandra* band must lie close to the peak of its νf_ν emission. This is because the X-ray photon index is $\sim$2 and the luminosity of this component at optical energies must be below the level of the optical emission detected downstream. The emission could in principle extend to energies higher than the *Chandra* band but this would require the presence of unrealistically energetic electrons. Because cooling of the X-ray emitting electrons is severe, even if we only consider the CMB photon energy density, these electrons are suffering strong cooling, which must be balanced by continuous reacceleration.

Finally, an account of most of the phenomenology may rest with the possibility that the entire radio–NIR-X-ray emission is synchrotron, and that the jet beam moves laterally with time to the west, implying that the maximum X-ray emission is the most recent and naturally further displaced from the AGN core. For this same reason (age), there is less IR and almost no radio emission in along this direction (the corresponding electron radiative times are longer). The fact that the radio emitting electrons have the longest radiative lifetime would then explain the displacement of the maximum emission at this frequency (and of the IR) to the east and the absence of X-rays in the same region (the X-ray emitting electrons have all cooled to lower energies). There is some indication of such a motion from the fact that the AGN core and the two lobes do not all line on a straight line.

To conclude, both the EC/CMB from a decelerating flow and synchrotron interpretation of the X-rays face important problems, although the EC/CMB model is more constrained and, therefore, easier to falsify, while the synchrotron interpretation can reproduce any observed emission by introducing additional electron populations as needed. A purely spectral discrimination between the synchrotron and IC models is not possible, as both can be made compatible with various X-ray slopes as well as the forms for the "valley" in between the X-ray and radio–IR components (see, e.g., Uchiyama et al. 2006, 2007; Jester et al. 2007; Hardcastle et al. 2004). The synchrotron interpretation, however, does not require beaming and is the only alternative among those examined that could produce detectable X-ray emission from the counter hot spot. Therefore, detection of bright X-ray emission from the counter hot spot in future X-ray observations would rule out any reasonable IC models for the hot spots of 3C 445. An additional test of the nature of the X-ray emission could come from future X-ray polarimeters like GEMS: while the synchrotron emission is expected to be highly polarized, the EC/CMB should produce negligible polarization (Begelman & Sikora 1987; McNamara et al. 2009; Y. Uchiyama & P. Coppi 2010, in preparation). An approach that can yield results with our current observational

capabilities is based on *Hubble Space Telescope* (*HST*) UV polarimetry: if the far UV emission is shown to be the low-energy tail of the X-ray component as is the case with 3C 273 (e.g., Jester et al. 2007), then UV *HST* imaging polarimetry of the hot spots will distinguish between the EC/CMB and synchrotron mechanisms (e.g., McNamara et al. 2009; Y. Uchiyama & P. Coppi 2010, in preparation).

We thank an anonymous referee for comments that significantly strengthened this paper. This work was supported at FIT and UMBC by the *Chandra* grant G07-8113A and the NASA LTSA grant NNX07AM17G. This project was also partially funded by a partnership between the National Science Foundation (NSF AST-0552798), Research Experiences for Undergraduates (REU), and the Department of Defense (DoD) ASSURE (Awards to Stimulate and Support Undergraduate Research Experiences) programs.

REFERENCES

Aloy, M. A., Ibáñez, J. M. A., Martí, J. M. A., Gómez, J.-L., & Müller, E. 1999, ApJ, 523, L125
Arshakian, T. G., & Longair, M. S. 2000, MNRAS, 311, 846
Begelman, M. C., & Sikora, M. 1987, ApJ, 322, 650
Blundell, K. M., Fabian, A. C., Crawford, C. S., Erlund, M. C., & Celotti, A. 2006, ApJ, 644, L13
Brunetti, G., Mack, K.-H., Prieto, M. A., & Varano, S. 2003, MNRAS, 345, L40
Cheung, C. C., Wardle, J. F. C., & Chen, T. 2005, ApJ, 628, 104
Deutsch, E. W. 1999, AJ, 118, 1882
Eracleous, M., & Halpern, J. P. 1994, ApJS, 90, 1
Erlund, M. C., Fabian, A. C., Blundell, K. M., Moss, C., & Ballantyne, D. R. 2007, MNRAS, 379, 498
Evans, D. A., et al. 2008, ApJ, 675, 1057
Fan, Z.-H., Liu, S., Wang, J.-M., Fryer, C. L., & Li, H. 2008, ApJ, 673, L139
Fanaroff, B. L., & Riley, G. M. 1974, MNRAS, 167, 31
Georganopoulos, M., & Kazanas, D. 2003, ApJ, 589, L5
Georganopoulos, M., & Kazanas, D. 2004, ApJ, 604, L81
Godfrey, L. E. H., et al. 2009, ApJ, 699, 31
Grandi, P., Guainazzi, M., Cappi, M., & Ponti, G. 2007, MNRAS, 381, L21
Hardcastle, M. J., Alexander, P., Pooley, G. G., & Riley, J. M. 1998, MNRAS, 296, 445
Hardcastle, M. J., Birkinshaw, M., Cameron, R. A., Harris, D. E., Looney, L. W., & Worrall, D. M. 2002, ApJ, 581, 948
Hardcastle, M. J., Harris, D. E., Worrall, D. M., & Birkinshaw, M. 2004, ApJ, 612, 729
Hardcastle, M. J., & Croston, J. H. 2005, MNRAS, 363, 649
Hardcastle, M. J., Croston, J. H., & Kraft, R. P. 2007, ApJ, 669, 893
Harris, D., & Krawczynski, H. 2006, ARA&A, 44, 463
Heavens, A. F., & Meisenheimmer, K. 1987, MNRAS, 225, 335
Jester, S., Meisenheimer, K., Martel, A. R., Perlman, E. S., & Sparks, W. B. 2007, MNRAS, 380, 828
Kassim, N. E., et al. 2007, ApJS, 172, 686
Kataoka, J., & Stawarz, Ł. 2005, ApJ, 622, 797
Kataoka, J. et al. 2008, ApJ, 685, 839
Kraft, R. P., Birkinshaw, M., Hardcastle, M. J., Evans, D. A., Croston, J. H., Worrall, D. M., & Murray, S. S. 2007, ApJ, 659, 1008
Lazio, T. J. W., Cohen, A. S., Kassim, N. E., Perley, R. A., Ericson, W. C., Carilli, C. L., & Crane, P. C. 2006, ApJ, 642, L33
Mack, K.-H., Prieto, M. A., Brunetti, G., & Orienti, M. 2009, MNRAS, 392, 705
McNamara, A. L., Kuncic, Z., & Wu, K. 2009, MNRAS, 395, 1507
Mehta, K. T., Georganopoulos, M., Perlman, E. S., Padgett, C. A., & Chartas, G. 2009, ApJ, 690, 1706
Meisenheimer, K., Roser, H.-J., Hiltner, P. R., Yates, M. G., Longair, M. S., Chini, R., & Perley, R. A. 1989, A&A, 219, 63
Migliori, G., Grandi, P., Palumbo, G. C., Brunetti, G., & Stanghellini, C. 2007, ApJ, 668, 203
Perlman, E. S., & Wilson, A. S. 2005, ApJ, 627, 140
Pounds, K. A. 1990, MNRAS, 242, 20p
Prieto, A., Brunetti, G., & Mack, K. 2002, Science, 298, 193
Sambruna, R. M., George, I. M., Mushotzky, R. F., Nandra, K., & Turner, T. J. 1998, ApJ, 495, 749
Sambruna, R. M., Reeves, J. N., & Braito, V. 2007, ApJ, 665, 1030
Spitkovsky, A. 2008, ApJ, 682, L5
Stawarz, Ł., Cheung, C. C., Harris, D. E., & Ostrowski, M. 2007, ApJ, 662, 213
Tavecchio, F., Cerutti, R., Maraschi, L., Sambruna, R. M., Gambill, J. K., Cheung, C. C., & Urry, C. M. 2005, ApJ, 630, 721
Tingay, S. J., Lenc, E., Brunetti, G., & Bondi, M. 2008, AJ, 136, 2473
Uchiyama, Y., et al. 2006, ApJ, 648, 910
Uchiyama, Y., et al. 2007, ApJ, 661, 719
Wilson, A. S., Young, A. J., & Shopbell, P. L. 2000, ApJ, 544, L27
Wilson, A. S., Young, A. J., & Shopbell, P. L. 2001, ApJ, 547, 740
Worrall, D. M. 2009, A&AR, 17, 1